Edge-NF$_x$ (x = 1 or 2) Protected Graphitic Nanoplatelets as a Stable Lithium Storage Material

Hyuk-Jun Noh[+],[a] Shenghong Liu[+],[b] Soo-Young Yu,[a] Qinghua Fan,[b] Feng Xiao,[b] Jiantie Xu, *[b] In-Yup Jeon,*[c] and Jong-Beom Baek*[a]

Edge-NF$_x$ (x = 1 or 2) protected graphitic nanoplatelets (NFGnPs) are synthesized for the first time as a stable anode material for lithium storage. The NFGnPs are prepared *via* mechanochemical reaction, by ball-milling graphite in the presence of nitrogen trifluoride (NF$_3$) gas. The average grain size of the NFGnPs is dramatically reduced compared to the starting graphite. The ball-milling effectively unzips graphitic C–C bonds, generating active carbon species (C$^\bullet$), which form edge C–NF$_x$ bonds and delaminate the graphite layers into a few layered NFGnPs. The resulting NFGnPs have a large specific surface area (671.0 m^2 g^{-1}). The edge functionalities of the NFGnPs consist of major C(C)=NF$_1$ and minor C–NF$_2$ moieties. Because of their large specific surface area, the NFGnPs display high average reversible capacities of 850.5, 722.4, 576.4, 482.0, 369.1, 229.7, 127.5 mAh g^{-1} at 0.2, 0.5, 1, 2, 5 and 10 C, respectively, with excellent rate capability. More importantly, due to the edge protection provided by the stable C(C)=NF$_1$ bonds (pseudo-aromatic), the NFGnPs maintain a high reversible charge capacity of 421.6 mAh g^{-1} at 2 C, with an initial capacity retention of 78.3% after 200 cycles.

1. Introduction

Since graphene's discovery,[1] numerous graphene-based materials have been developed for various applications. This wide utility is mainly due to graphene's unique properties, including a large theoretical surface area, high electrical conductivity and excellent thermal/chemical stability.[2–5] The study of graphene modification itself has attracted significant attention, to further tune graphene and realize desirable physicochemical properties.[6–8] Among the various approaches being explored, introducing heteroatoms into graphitic frameworks has proven to be particularly effective. This is because the difference in electronegativity between the carbon (C) and heteroatom (X) can induce charge polarization in the graphene, leading to modulated electronic states and improved electrochemical properties.

To date, several common approaches (*e.g.*, chemical vapor deposition method,[9–11] bottom-up synthesis,[12] thermal annealing[13] and wet chemical method[14–16]) have been employed to synthesize heteroatom-doped graphene-based materials. However, these approaches often require the use of expensive substrates or hazardous reagents. In addition, when introducing various heteroatoms, the processes are limited to forming application-specific C–X bonds with desired loading levels on the graphitic edge and/or basal plane.

To overcome these limitations, we have developed a simple, eco-friendly and low-cost mechanochemical reaction, which produces various heteroatom-doped graphitic nano-platelets (XGnPs).[17–22] This mechanochemical reaction not only enables the selective introduction of desired heteroatom(s) on the edges of the graphitic nanoplatelets (GnPs), but also preserves their integrity in the basal plane, ensuring electronic conductivity.

Fluorine (F) has the highest electronegativity (χ = 3.98) in the periodic table. As expected, the large difference in electronegativity (1.43) between C and F allows the F to polarize the adjacent C atoms to a great extent, and then facilitates high mass adsorption/storage and release.[23,24] In our previous study, edge-fluorinated graphitic nanoplatelets (FGnPs) were successfully prepared by ball-milling graphite in the presence of diluted fluorine (F$_2$) gas (20%) in argon.[20] The resulting FGnPs displayed rich and strong covalent C–F bonds at their edges. The rich C–F edges and highly crystalline basal planes enhance the FGnPs, and as electrodes they showed outstanding performance in dye-sensitized solar cells (DSSCs) and lithium-ion batteries (LIBs). Despite this, F$_2$ gas is too dangerous to use as the starting material to produce FGnPs. This fact motivated our search for alternative methods to mass produce fluorinated GnPs.

[a] H.-J. Noh,[+] S.-Y. Yu, Prof. J.-B. Baek
School of Energy and Chemical Engineering/
Center for Dimension-Controllable Organic Frameworks
Ulsan National Institute of Science and Technology (UNIST)
50 UNIST, Ulsan 44919, South Korea
E-mail: jbbaek@unist.ac.kr
[b] S. Liu,[+] Dr. Q. Fan, Dr. F. Xiao, Prof. J. Xu
Guangdong Provincial Key Laboratory of Atmospheric Environment and Pollution Control
School of Environment and Energy,
South China University of Technology
Guangzhou 510640, China
E-mail: jiantiexu@scut.edu.cn
[c] Prof. I.-Y. Jeon
Department of Chemical Engineering,
Wonkwang University
460, Iksandae-ro, Iksan, Jeonbuk 54538, Korea
E-mail: iyjeon79@wku.ac.kr
[+] These authors contributed equally to this work.

In this paper, we introduce a safe and facile 'one-step' approach to prepare edge-selectively NF$_x$-protected GnPs (NFGnPs) by ball-milling graphite in the presence of nitrogen trifluoride (NF$_3$) gas instead of the very dangerous F$_2$ gas as a fluorinating agent. In addition to the improved safety, using NF$_3$ gas produced NFGnPs with unique C-NF$_x$ ($x=1$ or 2) bonds at their edges and a high specific surface area (671.0 m^{2}g^{-1}). As a result, the NFGnPs displayed superior lithium storage properties, including high average capacity (*e.g.*, 850.5 mAhg^{-1} at 0.2 C), excellent rate capability (*e.g.*, 229.7, 127.5 mAhg^{-1} at 5 and 10 C, respectively). More importantly, due to the edge protection provided by the stable C(C)=NF$_1$ bonds (pseudo-aromatic), the NFGnPs demonstrated long cycling stability (*e.g.*, 421.6 mAhg^{-1} at 2 C with an initial capacity retention of 78.3% after 200 cycles).

2. Results and Discussion

As shown in Figure 1a, the NFGnPs were produced *via* mechanochemical reaction by ball-milling graphite in the presence of NF$_3$ gas. During the reaction, graphitic layers are unzipped, generating active carbon species (C$^\bullet$) to react with NF$_3$ to yield NFGnPs (Figure S1). The remnant active species are completely terminated by air and moisture during the subsequent work-up procedures.

As a reference for comparison, edge-hydrogenated GnPs (HGnPs) were also prepared to decorate C–H bonds along their edges.[18]

The most important advantage of using nitrogen trihalides (NF$_3$, NCl$_3$, NBr$_3$ and NI$_3$), specifically, using NF$_3$ gas over fluorine (F$_2$) gas as a fluorinating agent, is safety. NF$_3$ gas is a non-flammable reagent and is also easy to handle, store and transport at ambient temperature.[25]

At the same time, a very large number of nitrogen (N)-doped carbon materials have been investigated as promising electrode candidates for various energy and storage systems.[9,26–28] Their attractive performance is mainly due to the difference in electronegativity between the constituent nitrogen ($\chi=3.04$) and carbon ($\chi=2.55$), which can be exploited to modulate the electronic structure and physicochemical properties of the carbon frameworks. Recently, several reports have also confirmed that N and F dual-doped graphene-based materials have displayed high electrochemical activity due to synergistic effects induced by the electronegative N and F atoms.[29–32] In these previous results, however, the synthesis routes of the N and F dual-doped graphene-based materials often involved tedious "multistep" procedures. In addition, the doping levels of the N and F atoms have not been satisfactory. Under these circumstances, the mass production of NFGnPs using NF$_3$ gas could be a potentially useful method of synthesizing new N and F dual-doped graphene-based materials for practical applications.

The morphologies of the reference HGnPs (Figure 1c) and NFGnPs (Figure 1d) were observed before and after ball-milling of the graphite (Figure 1b), by scanning electron microscopy (SEM). The starting graphite had a large grain size (<150 μm), but they were dramatically reduced in the HGnPs and NFGnPs to a few micrometers (<5 μm). These results suggest that the
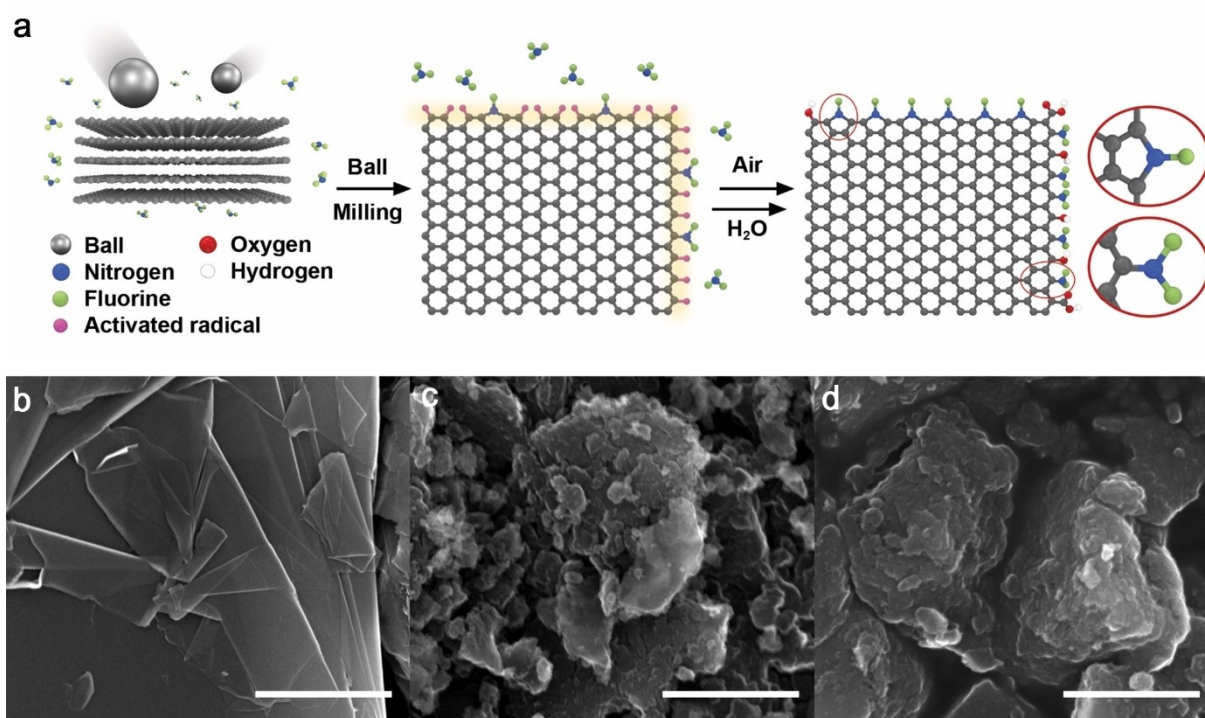

Figure 1. a) Schematic depiction of the process used to prepare NFGnPs by mechanochemical reaction with graphite and nitrogen trifluoride (NF$_3$). SEM images: b) pristine graphite, c) HGnPs and d) NFGnPs. All scale bars are 1 μm.

Batteries & Supercaps

Articles
doi.org/10.1002/batt.202000056

Chemistry Europe
European Chemical
Societies Publishing

mechanochemical ball-milling unzipped graphitic C–C bonds, generating active carbon species (C•) to react with NF_3 to form C–NF_x bonds (Figure S1), while delaminating the graphitic layers into a few layers of NFGnPs.

High-resolution TEM (HR-TEM) was used to examine the crystallinity of the basal plane of the NFGnPs. As shown in Figure S2, the NFGnPs exhibited less than seven graphitic layers (red arrow, Figure S2b) with crystalline honeycomb lattice patterns (right bottom inset, Figure S2b), as can be seen in the fast Fourier transform (FFT) image (right top inset, Figure S2b). This could be due to the high degree of crystalline structure of NFGnPs, even after NF_3 was introduced at their edges by the ball-milling process. The presence of nitrogen and fluorine was confirmed by energy dispersive X-ray spectra (EDX) using SEM (Figure S3). The EDX elemental mapping images of the NFGnPs showed uniformly distributed N and F, indicating NF_3 had been introduced at the edges (Figure S4). A detailed summary of the quantitative elemental contents of carbon, oxygen, nitrogen and fluorine from the EDX results are provided in Table S1.

The degree of exfoliation could be estimated by analyzing powder X-ray diffraction (PXRD) patterns before and after mechanochemical reaction. Graphite has a strong intensity (002) peak at 26.5° (d-spacing = 3.34 nm), and this almost disappeared in the NFGnPs (Figure 2a), indicating a significant degree of delamination. Furthermore, the (002) peak was shifted to a lower angle (21.1°) and broadened (inset, Figure 2a), suggesting that the interlayer distance of the NFGnPs was widened (d-spacing = 4.21 nm) by the edge-functionalization and thus edge-lifting. The degree of exfoliation was simply calculated by Branauer-Emmett-Teller (BET) analysis. Compared to the BET specific surface area (2.8 $m^2 g^{-1}$) of the pristine graphite, the NFGnPs exhibited approximately 240 times increase in specific surface area (671.0 $m^2 g^{-1}$) (Figure S5, detailed values are summarized in Table S2). Considering the maximum surface area of a single graphene layer (2630 $m^2 g^{-1}$), the average number of layers in the solid-state NFGnPs can be simply calculated to be ∼ 4.0 (2630/671).

For more detailed insight into the chemical bonding nature of the NFGnPs, Fourier-transform infrared (FT-IR) was utilized (Figure 2b). The strong peaks at 1589 and 1205 cm^{-1} are associated with C=C and N–F/C–O bonds, respectively. The relatively weak peaks at 1712, 1620, and 745 cm^{-1} are, respectively, assignable to C=O, C=N, and bending C=N. The C=N bonds indicate a pseudo-aromatic nature of C(C)=NF_1 bond (Figure S1). In addition, the peaks at 2853 and 2918 cm^{-1} are related to sp^3 C–H and sp^2 C–H, respectively, which are formed by reactions between the remaining active carbon species and moisture during the work-up procedures.

To further explore the chemical bonding states of the NFGnPs, X-ray photoelectron spectroscopy (XPS) was applied. Compared to pristine graphite, the NFGnPs exhibited additional N 1s, O 1s and sharp F 1s peaks (Figure 2c). In the high-resolution XPS spectra, the C 1s spectrum of NFGnPs can been deconvoluted into four different peaks, C=C (284.4 eV), C–O (285.6 eV), C–N (286.9 eV), C=O (289.5 eV) and π-π* (292.3 eV) (Figure S6a).[32,33] The N 1s spectrum of the NFGnPs are split into four different peaks, pyridinic-N (398.8 eV), NF_1 (399.6 eV),

pyrrolic-N (400.6 eV) and NF_2 (404.4 eV) (Figure 2d). These results are in good agreement with the suggested edge structures of the NFGnPs in Figure 1a and Figure S1. Furthermore, the O 1s peak can be divided into three different peaks of C=O (531.4 eV), C–O (532.8 eV) and adsorbed H_2O (537.4 eV) (Figure S6b).[33] The trace amount of H_2O is due to the hygroscopic nature of the NFGnPs after the remnant active carbon species being terminated with air (e.g., O_2) and moisture (H_2O).

In addition to the high-resolution XPS spectra of C 1s, N 1s and O 1s, the deconvoluted F 1s peaks are part of a major C (C)=NF_1 bond at 687.6 eV and a minor C–NF_2 bond at 690.5 eV, indicating two types of NF_x bonding state at the edge of the NFGnPs (Figure 2e). Compared to the previously reported C–F bonds forming the FGnPs,[20] the intensity of the F 1s is much stronger in the NFGnPs, due to the formation of C–NF_x (x = 1 or 2) bonds, which are much more accessible than C–F bonds. This suggests a straightforward method for the production of NF_x doped GnPs. Furthermore, the major C(C)=NF_1 bonds along the armchair edges of NFGnPs possess pseudo-aromatic (4n + 2) π nature, anticipating their electrochemical stability (Figure S1).

Strong evidence of the NF_x-functionalization was further studied using the solid-state ^{19}F cross-polarization magic-angle spinning (CP-MAS) nuclear magnetic resonance (NMR) method (Figure 2f). The two broad peaks at −63.3 and −89.8 ppm can be assigned to the C(C)=NF_1 and C–NF_2 bonds, respectively. These two peaks are positioned at higher chemical shifts, which suggest more de-shielding than the C–F bonds in the FGnPs.[20] This is because N is more electronegative than C, and pulls electron density. In addition, a strong NF_1 stretch band was observed as a dominant peak with a minor NF_2 peak, in accordance well with the FT-IR (Figure 2b) and XPS results (Figure 2e). Thus, the introduction of NF_x at the edges of NFGnPs in forms of C(C)=NF_1/C–NF_2 could be confirmed (Figure S1).

Raman spectroscopy was used to reveal the structural difference between the pristine graphite and NFGnPs. While the pristine graphite showed no D band peak, the NFGnPs displayed a sharp D band peak at around 1346 cm^{-1} and a high I_D/I_G ratio of 1.29. This is contributed to the high edge to basal ratio from the dramatic grain size reduction and large edge distortion from NF_x-functionalization along the edge of NFGnPs (Figure S7).

The prepared NFGnPs showed high dispersibility in most protic and polar aprotic solvents, due to the contributions of enhanced edge polarity (enthalpy) and size reduction (entropy) (Figure S8). To evaluate their stability in dispersion, ζ-potential measurements were carried out at different concentrations using NMP as the solvent (Figure S9). The NFGnPs had high absolute values of the ζ-potential in the range of −30.7 to −46.6 mV. The values were higher than ±30 mV, implicating a stable dispersion.[34] Furthermore, the surface polarity of the NFGnPs was also examined by contact angle measurements (Figure S10). The average contact angles of the silicon wafer (reference) and NFGnPs were found to be 48.3 and 91.6°, respectively.
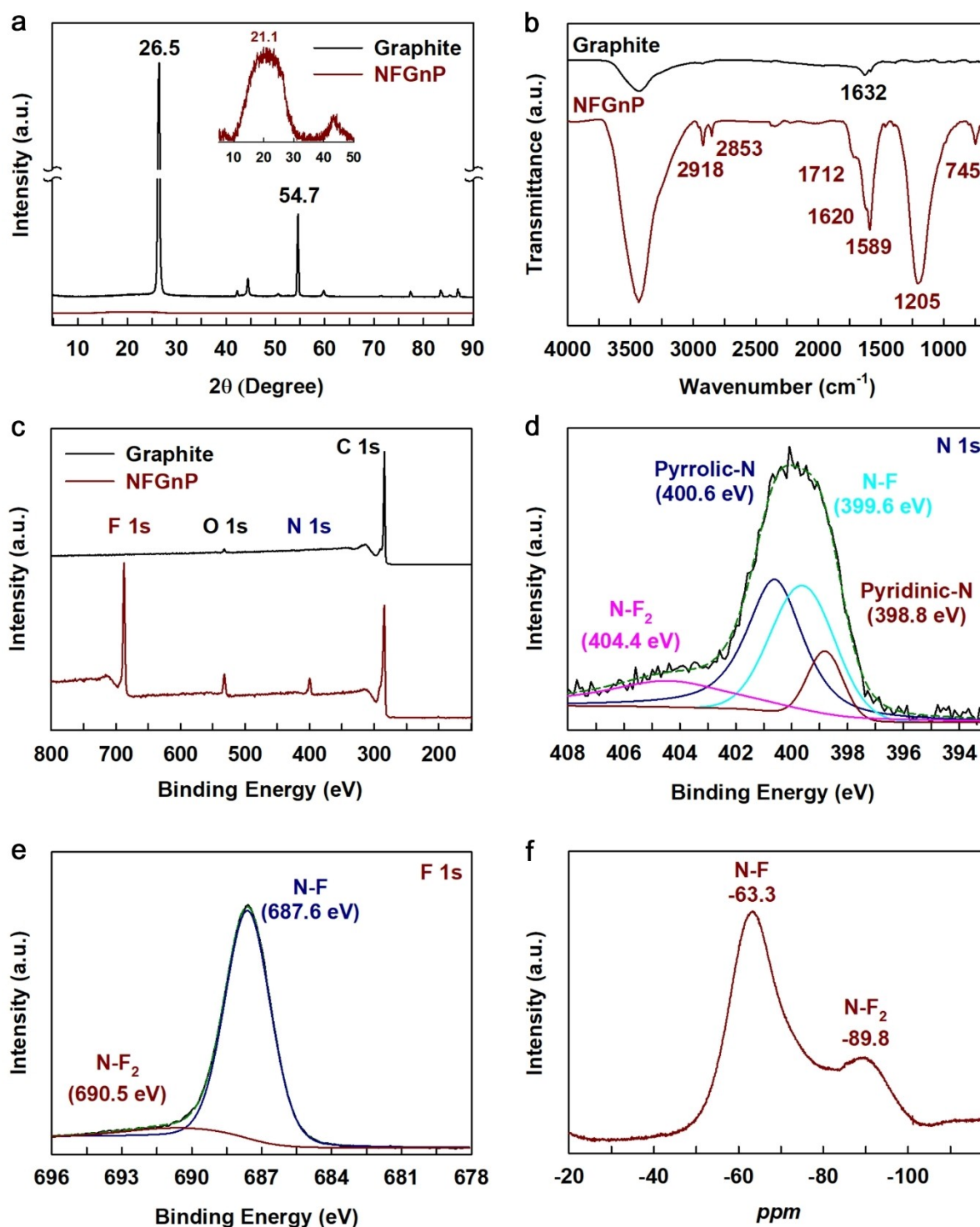
Figure 2. Characterizations of the pristine graphite and NFGnPs. a) PXRD patterns b) FT-IR spectra. c) XPS survey spectra. High-resolution XPS spectra: d) N 1s; e) F 1s. f) ^{19}F CP-MAS NMR spectrum of NFGnPs.

Graphite is the most commonly used anode for LIBs, and has dominated that market for nearly 30 years. However, its low theoretical capacity of 372 mAh g^{-1} and poor rate capability severely limit its application in high-demand energy storage systems such as electric vehicles and stationary energy storage grids.[35,36]

FGnPs have displayed outstanding lithium storage properties and stability, due to their large specific surface area, high-quality graphitic basal plane and edge-protection provided by the most stable C—F bonds, making them a promising anode material.[20] However, using dangerous F$_2$ gas limits the practical uses of FGnPs. NFGnPs, prepared using NF$_3$ rather than F$_2$, are

of much more practical interest for use as an anode material for LIBs.

Figure 3 a shows the initial 5 cycle discharge-charge profiles of NFGnPs measured at 0.1 C (assumption 1 C = 500 mA g^{-1}) in the voltage range of 0.02–3 V. As can be seen, the NFGnPs display the typical electrochemical behavior of carbonaceous materials, which is different from the graphite.[20,35,37] During the discharge process in the first cycle, the NFGnPs exhibit an obvious plateau at ~1 V. This corresponds to the first reduction peak at ~0.8 V in the cyclic voltammetry (CV) curves at a scan rate of 0.1 mV s^{-1} (Figure 3b). This is mainly due to the formation of a solid electrolyte interface (SEI) film, caused by irreversible electrolyte decomposition. In the following three cycles, the pronounced reduction peaks disappear at ~1 V, and highly overlapped discharge-charge profiles (Figure 3a) appear in the CV curves (Figure 3b). All of these results support the formation of a strong and dense SEI film in the first cycle, and the excellent structural stability of the electrodes during the Li$^+$ insertion/extraction process.

At higher C-rates from 0.2 to 10 C, the NFGnPs still present the typical discharge-charge profiles of carbonaceous materials (Figure 3c). The rate capability of the reference HGnPs and NFGnPs are compared in Figure 3d at various C-rates from 0.1

to 10 C in the voltage range of 0.02–3 V. The NFGnPs exhibit a higher initial discharge capacity of 1804.5 mAh g^{-1} at 0.1 C with an initial Coulombic efficiency (CE) of 48.8%, which are higher values than that of the HGnPs (1667.0 mAh g^{-1} and 48.0%). The low initial CE is mainly due to the formation of the SEI film. At higher C-rates from 0.2 to 10 C, the NFGnPs display higher average capacities, of 850.5, 722.4, 576.4, 482.0, 369.1, 229.7, 127.5 mAh g^{-1} at 0.2, 0.5, 1, 2, 5 and 10 C, respectively, as well as excellent rate capability (inset of Figure 3d), compared to the HGnPs.

In order to further assess the cycling stability of the HGnPs and NFGnPs, the cells measured at 0.5 C for 200 cycles were compared (Figure 3e). The NFGnPs delivered a higher initial charge capacity of 703.7 mAh g^{-1} and maintained 484.6 mAh g^{-1} after 200 cycles, with a higher initial capacity retention of 68.9%, compared to those of the HGnPs (327.3 mAh g^{-1} and 63.2%). At 2 C, the NFGnPs were still able to deliver a higher reversible charge capacity of 421.6 mAh g^{-1} after 200 cycles, with an initial capacity retention of 78.3%. It should be noted that a slight growing in capacity for NFGnPs in the initial cycles is mainly because of the electrode-electrolyte activation. Despite the differences in capacity and capacity retention, both the HGnPs and NFGnPs exhibited high average
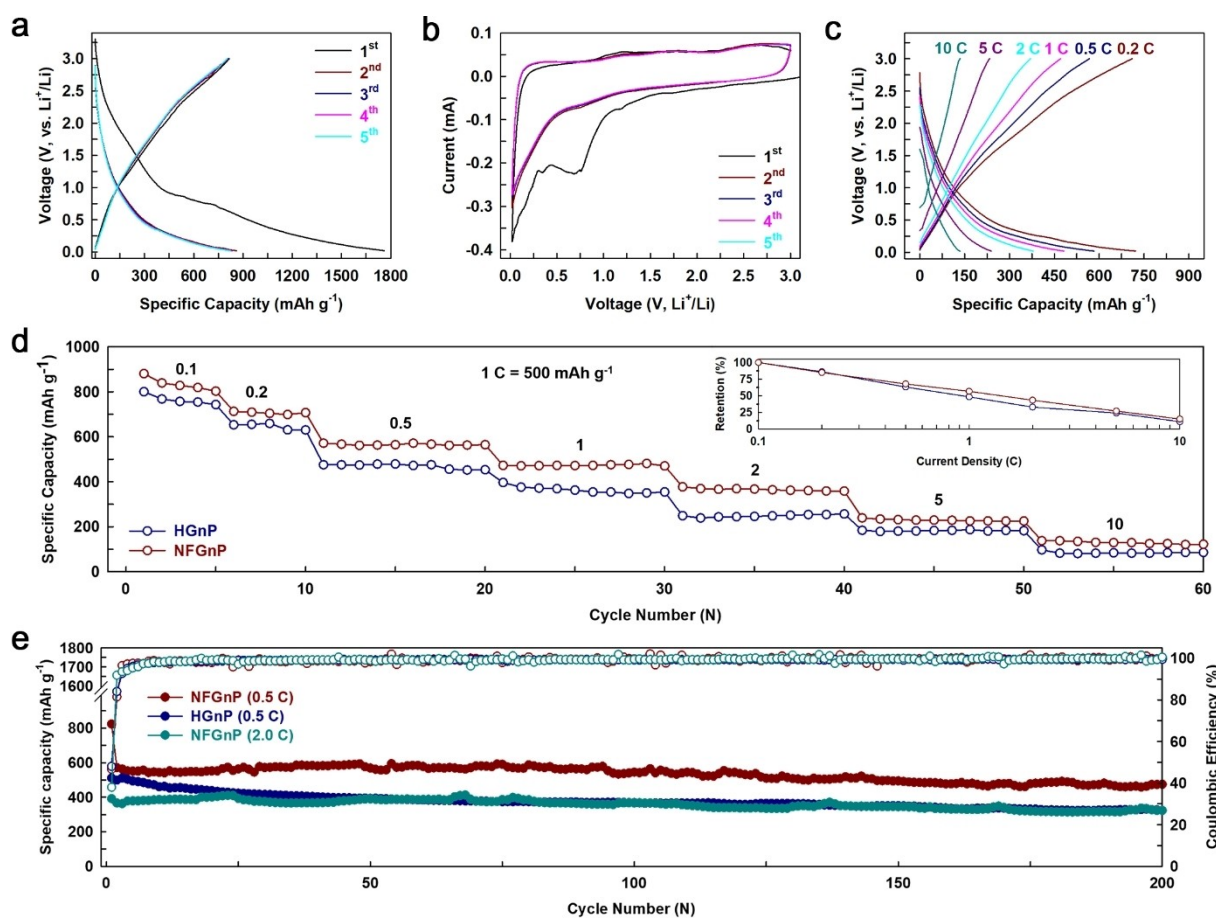

Figure 3. a) Initial 5 discharge-charge profiles of the NFGnPs at 0.1 C. b) Initial 5 cyclic voltammetry (CV) cycles at 0.1 mV s^{-1} and c) discharge-charge profiles of NFGnPs at various C-rates from 0.2 to 10 C. d) Rate capability measurements of NFGnPs and HGnPs. Inset of (d): Capacity retention vs. C-rate. e) Cycling performance of NFGnPs and HGnPs.

Coulombic efficiencies of ~99.6% (Figure 3e) over the 200 cycles, once again indicating the highly stable structures of the GnPs during each lithiation-delithiation process.

In order to better understand the kinetics of the NFGnPs, electrochemical impedance spectroscopy (EIS) measurements were carried out (Figure 4a). The Nyquist plots of the NFGnPs, which were measured at 0.5 C for 5 cycles and kept at the discharged state of 1.0 V (vs. Li/Li$^+$), were obtained at various temperatures between 301.05 and 326.05 K. The plots consist of a semicircle at high frequency, a semicircle at medium frequency and a linear region. They can be, respectively, assigned to the internal resistance electrolyte, solid electrolyte interphase (SEI) film resistance (R_{SEI}), charge transfer resistance (R_{ct}), and ionic diffusion impedance through the bulk of the active material (W). The double semicircles in the high-medium frequency regions were further confirmed with the NFGnPs electrode measured after 100 cycles (Figure 4b). The R_{ct} and apparent activation energies (E_a) are key indicators for the electrode kinetics. An equivalent circuit (inset, Figure 4a) was fabricated to analyze R_{ct}. Tables S3 and S4 list the fitted R_e, R_s and R_{ct} results. As shown in Tables S3 and S4, and Figure 4c (top), the R_{ct} significantly decreased as the temperature increased. This is mainly due to the evaluated charge transfer

kinetics. The E_a of the NFGnPs electrode was calculated using the Arrhenius Equations (1) and (2) as follows:[38]

$$i_o = RT/(nFR_{ct}) \tag{1}$$

$$i_o = A \exp(-E_a/RT) \tag{2}$$

where i_0, A, R, T (K), n, F and E_a are the exchange current, a temperature-independent coefficient, the gas constant, the absolute temperature, the number of transferred electrons, Faraday constant and apparent activation energy, respectively. The apparent activation energy of the NFGnPs was fitted to 34.6 kJ mol^{-1} (Figure 4d), which is lower than the 38.7 kJ mol^{-1} of the HGnPs.[39] The lower activation energy indicates there is a more facile insertion-extraction of Li$^+$ during the discharge-charge process. Moreover, the value of R_{ct} experiences an obvious decrease over the first 100 cycles (Figure 4c (bottom)). However, the R_{ct} of the NFGnPs remains almost constant for the next 100 cycles. This is mainly due to the electrode-electrolyte activation during the initial cycles, in which the electrolytes gradually penetrate the accessible surface areas of the electrode.
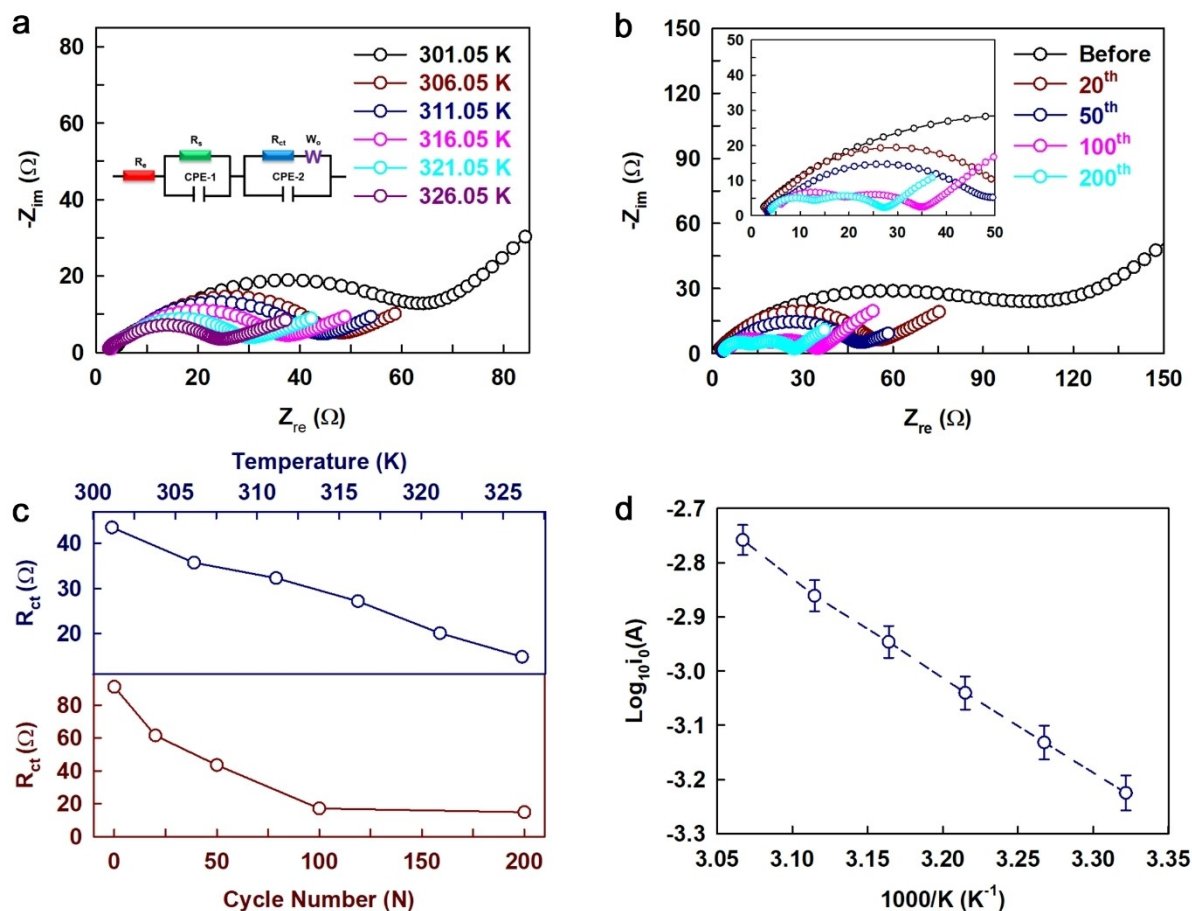

Figure 4. Nyquist plots of the NFGnPs measured a) at the discharged state of 1.0 V (vs. Li/Li$^+$) at different temperatures and b) before cycling and after different cycles. Inset in (a): equivalent circuit for EIS analysis. c) R_{ct} calculated from the (a-top) and (b-bottom) EIS fitting. d) Arrhenius plots of log i_0 versus 1/T of the NFGnPs. The lines are the linear fitting results.

3. Conclusions

In summary, we report for the first time NF$_x$-protected graphitic nanoplatelets (NFGnPs) synthesized *via* a facile mechanochemical reaction, driven by the one-step ball-milling of graphite in the presence of nitrogen trifluoride (NF$_3$) gas. The process avoids the use of hazardous chemicals such as HF and/or F$_2$. The resulting NFGnPs were functionalized with NF$_1$/NF$_2$ bonds at their edges, which induced delamination, imparted charge polarization and widened interlayer distances. In addition, the NFGnPs had a smaller grain size and much larger specific surface area than pristine graphite, while preserving the graphitic basal plane.

When the NFGnPs were tested as an anode material for LIBs, they displayed high average capacities of 850.5, 722.4, 576.4, 482.0, 369.1, 229.7, 127.5 mAh g^{-1} at 0.2, 0.5, 1, 2, 5 and 10 C, respectively. In addition, the NFGnPs showed a higher initial charge capacity of 703.7 mAh g^{-1} and an initial capacity retention of 68.9% (484.6 mAh g^{-1}) after 200 cycles, compared with the reference HGnPs (63.2% and 327.3 mAh g^{-1}). More importantly, the NFGnPs exhibited a higher reversible charge capacity of 421.6 mAh g^{-1} at 2 C with an initial capacity retention of 78.3% after 200 cycles.

We anticipate that NFGnPs, with N and F dual-doped edges, will provide a new platform for the practical mass production of functional carbon materials.

Experimental Section

Materials

Graphite was used as received from Alfa Aesar (Natural, 100 mesh, 99.9995% metals basis). NF$_3$ was purchased from RIGAS and used as received. All other chemicals were supplied by Aldrich Chemical Inc. and used without further purification, unless otherwise specified.

Synthesis of HGnPs and NFGnPs

HGnPs were produced by following our reported procedures.[18] Both HGnPs and NFGnPs were prepared by ball-milling graphite in the presence of corresponding gas (H$_2$ or NF$_3$) in a planetary ball-mill machine (Pulverisette 6, Fritsch). The pristine graphite (5.0 g) was charged in a stainless steel ball-mill reactor, containing stainless steel balls (500.0 g, diameter: 5 mm). The capsule was sealed after five charging-discharging cycles of argon gas to remove air. Then, the capsule was charged with hydrogen gas (H$_2$, 10 bar) for HGnPs or nitrogen trifluoride (NF$_3$, 10 bar) for NFGnPs. Then, it was placed in the planetary ball-mill machine and agitated at 500 rpm for 48 h. The resultant products were repeatedly washed with 1 M aq. HCl solution to deactivate residual active species as well as to remove metallic impurities, if any. Furthermore, the products were Soxhlet extracted with water and methanol for two days each. The final products were freeze dried at −120°C under reduced pressure (0.05 mmHg) for 48 h and then yielded 5.32 g (0.32 g weight increase) for HGnPs and 8.61 g (3.61 g weight increase) for NFGnPs.

Instrumentation

Powder X-ray diffraction (PXRD) data were conducted on a High-Power X-Ray Diffractometer D/MAX 2500 V/PC (Cu–Kα radiation, 40 kV, 200 mA, $\lambda = 1.54056$ Å) (Rigaku Inc., Japan). Fourier transform infrared (FT-IR) spectra were obtained on a Spectrum 100 (Perkin-Elmer, USA) with a KBr pellet. Magic-angle spinning (MAS) nuclear magnetic resonance (NMR) spectrum was recorded using an Agilent V NMRS 600 spectrometer. The Raman spectra were obtained on a confocal Raman microscopy (WITec Alpha300R) with laser wavelength of 532 nm. X-ray photoelectron spectroscopy (XPS) was measured by an X-ray Photoelectron Spectrometer Thermo Fisher K-alpha (UK). Scanning electron microscopy (SEM) images were taken with a Field Emission Scanning Electron Microscope (Nanonova 230 FEI, USA). High-resolution transmission electron microscopy (HR-TEM) was performed using a JEM-2100F microscope (JEOL, Japan) under an operating voltage of 200 keV. The TEM specimens were prepared by dropping dispersed ethanol solution on holey carbon TEM grid (Ted Pella Inc., 200 Mesh Copper Grid) and dried in oven at 40°C under reduced pressure. The specific surface area was measured by nitrogen adsorption and desorption isotherms using the Brunauer-Emmett-Teller (BET) method on BELSORP-max (BEL Japan Inc., Japan). Elementary analysis (EA) were carried out using a Flash 2000 Analyzer (Thermo Scientific Inc., USA). ζ-potential values were measured using a Malvern Zetasizer (Nano ZS, Malvern Instruments). Contact angle measurements were performed on a Krüss DSA 100 contact angle analyzer. Sample solutions were coated on a silicon (Si) wafer.

Electrochemical measurements

The electrochemical characterization of the NFGnPs was performed using CR2032 coin-type cells. The electrodes were prepared by blending the active materials, carbon black and polyvinylidene difluoride (PVDF) binder, in a mass ratio of 8:1:1, respectively. The N-methyl-2-pyrrolidone (NMP) was used as the blending solvent. The obtained slurry was coated on Cu foil and then dried in a vacuum oven at 90°C for 24 h. The electrode mass of punched electrode pellet was controlled at ~1.0 mg cm^{-2}. The coin-type cells were assembled in glove box with high-purity Ar-filled atmosphere. The coin cells fabricated using lithium pellet as the counter and reference electrode, as-prepared electrode as the working electrode, a porous polypropylene as the separator and 1 M LiPF$_6$ in a mixture of ethylene carbonate (EC)/diethyl carbonate (DEC) (1/2, v/v) as an electrolyte. The fabricated coin-cells were discharged/charged using Land® battery tester system (Wuhan, China). Electrochemical impedance spectroscopy (EIS) and cyclic voltammetry (CV) were measured on AUTOLAB PGSTAT302N electrochemical workstation (Metrohm, Netherlands).

Conflict of Interest

The authors declare no conflict of interest.

[1] K. S. Novoselov, *Science* **2004**, *306*, 666.
[2] T. O. Wehling, K. S. Novoselov, S. V. Morozov, E. E. Vdovin, M. I. Katsnelson, A. K. Geim, A. I. Lichtenstein, *Nano Lett.* **2008**, *8*, 173.
[3] X. Wang, G. Sun, P. Routh, D.-H. Kim, W. Huang, P. Chen, *Chem. Soc. Rev.* **2014**, *43*, 7067.
[4] A. Fasolino, J. H. Los, M. I. Katsnelson, *Nat. Mater.* **2007**, *6*, 858.
[5] M. D. Stoller, S. Park, Y. Zhu, J. An, R. S. Ruoff, *Nano Lett.* **2008**, *8*, 3498.
[6] Y. Xu, Z. Liu, X. Zhang, Y. Wang, J. Tian, Y. Huang, Y. Ma, X. Zhang, Y. Chen, *Adv. Mater.* **2009**, *21*, 1275.
[7] Y. Xu, H. Bai, G. Lu, C. Li, G. Shi, *J. Am. Chem. Soc.* **2008**, *130*, 5856.
[8] S. Stankovich, R. D. Piner, S. T. Nguyen, R. S. Ruoff, *Carbon* **2006**, *44*, 3342.
[9] L. Ci, L. Song, C. Jin, D. Jariwala, D. Wu, Y. Li, A. Srivastava, Z. F. Wang, K. Storr, L. Balicas, F. Liu, P. M. Ajayan, *Nat. Mater.* **2010**, *9*, 430.
[10] D. Wei, Y. Liu, Y. Wang, H. Zhang, L. Huang, G. Yu, *Nano Lett.* **2009**, *9*, 1752.
[11] C.-K. Chang, S. Kataria, C.-C. Kuo, A. Ganguly, B.-Y. Wang, J.-Y. Hwang, K.-J. Huang, W.-H. Yang, S.-B. Wang, C.-H. Chuang, M. Chen, C.-I. Huang, W.-F. Pong, K.-J. Song, S.-J. Chang, J.-H. Guo, Y. Tai, M. Tsujimoto, S. Isoda, C.-W. Chen, L.-C. Chen, K.-H. Chen, *ACS Nano* **2013**, *7*, 1333.
[12] L. Tang, X. Li, R. Ji, K. S. Teng, G. Tai, J. Ye, C. Wei, S. P. Lau, *J. Mater. Chem.* **2012**, *22*, 5676.
[13] Z.-S. Wu, W. Ren, L. Xu, F. Li, H.-M. Cheng, *ACS Nano* **2011**, *5*, 5463.
[14] Z.-S. Wu, A. Winter, L. Chen, Y. Sun, A. Turchanin, X. Feng, K. Müllen, *Adv. Mater.* **2012**, *24*, 5130.
[15] H.-L. Guo, P. Su, X. Kang, S.-K. Ning, *J. Mater. Chem. A* **2013**, *1*, 2248.
[16] Y. Zhang, K. Fugane, T. Mori, L. Niu, J. Ye, *J. Mater. Chem.* **2012**, *22*, 6575.
[17] I.-Y. Jeon, H.-J. Choi, M. Choi, J.-M. Seo, S.-M. Jung, M.-J. Kim, S. Zhang, L. Zhang, Z. Xia, L. Dai, N. Park, J.-B. Baek, *Sci. Rep.* **2013**, *3*, 1810.
[18] I.-Y. Jeon, H.-J. Choi, S.-M. Jung, J.-M. Seo, M.-J. Kim, L. Dai, J.-B. Baek, *J. Am. Chem. Soc.* **2013**, *135*, 1386.
[19] I.-Y. Jeon, M. Choi, H.-J. Choi, S.-M. Jung, M.-J. Kim, J.-M. Seo, S.-Y. Bae, S. Yoo, G. Kim, H. Y. Jeong, N. Park, J.-B. Baek, *Nat. Commun.* **2015**, *6*, 7123.
[20] I.-Y. Jeon, M. J. Ju, J. Xu, H.-J. Choi, J.-M. Seo, M.-J. Kim, I. T. Choi, H. M. Kim, J. C. Kim, J.-J. Lee, H. K. Liu, H. K. Kim, S. Dou, L. Dai, J.-B. Baek, *Adv. Funct. Mater.* **2015**, *25*, 1170.
[21] I.-Y. Jeon, S. Zhang, L. Zhang, H.-J. Choi, J.-M. Seo, Z. Xia, L. Dai, J.-B. Baek, *Adv. Mater.* **2013**, *25*, 6138.
[22] J. Xu, I.-Y. Jeon, H.-J. Choi, S.-J. Kim, S.-H. Shin, N. Park, L. Dai, J.-B. Baek, *2D Mater.* **2016**, *4*, 014002.
[23] F.-G. Zhao, G. Zhao, X.-H. Liu, C.-W. Ge, J.-T. Wang, B.-L. Li, Q.-G. Wang, W.-S. Li, Q.-Y. Chen, *J. Mater. Chem. A* **2014**, *2*, 8782.
[24] X. Chia, A. Ambrosi, M. Otyepka, R. Zbořil, M. Pumera, *Chem. Eur. J.* **2014**, *20*, 6665.
[25] B. Golja, J. A. Barkanic, A. Hoff, *Microelectron. J.* **1985**, *16*, 5.
[26] Y. Shao, S. Zhang, M. H. Engelhard, G. Li, G. Shao, Y. Wang, J. Liu, I. A. Aksay, Y. Lin, *J. Mater. Chem.* **2010**, *20*, 7491.
[27] M. Deifallah, P. F. McMillan, F. Corà, *J. Phys. Chem. C* **2008**, *112*, 5447.
[28] Z. Yan, Q.-W. Yang, Q. Wang, J. Ma, *Chin. Chem. Lett.* **2020**, *31*, 583.
[29] X. Yue, S. Huang, Y. Jin, P. K. Shen, *Catal. Sci. Technol.* **2017**, *7*, 2228.
[30] S. Huang, Y. Li, Y. Feng, H. An, P. Long, C. Qin, W. Feng, *J. Mater. Chem. A* **2015**, *3*, 23095.
[31] J. Zhang, L. Dai, *Angew. Chem. Int. Ed.* **2016**, *55*, 13296.
[32] S. G. Peera, A. K. Sahu, A. Arunchander, S. D. Bhat, J. Karthikeyan, P. Murugan, *Carbon* **2015**, *93*, 130.
[33] L. Stobinski, B. Lesiak, A. Malolepszy, M. Mazurkiewicz, B. Mierzwa, J. Zemek, P. Jiricek, I. Bieloshapka, *J. Electron Spectrosc. Relat. Phenom.* **2014**, *195*, 145.
[34] D. H. Everett, *Basic Principles of Colloid Science*, The Royal Society of Chemistry, **1988**, 76.
[35] F. Xiao, X. Chen, J. Zhang, C. Huang, T. Hu, B. Hong, J. Xu, *J. Energy Chem.* **2020**, *48*, 122.
[36] M. Wu, J. Liao, L. Yu, R. Lv, P. Li, W. Sun, R. Tan, X. Duan, L. Zhang, F. Li, J. Kim, K. H. Shin, H. Seok Park, W. Zhang, Z. Guo, H. Wang, Y. Tang, G. Gorgolis, C. Galiotis, J. Ma, *Chem. Asian J.* **2020**, *15*, 995.
[37] R. Raccichini, A. Varzi, S. Passerini, B. Scrosati, *Nat. Mater.* **2014**, *14*, 271.
[38] J. Xu, S.-L. Chou, Q.-f. Gu, H.-K. Liu, S.-X. Dou, *J. Power Sources* **2013**, *225*, 172.
[39] J. Xu, J. Ma, Q. Fan, S. Guo, S. Dou, *Adv. Mater.* **2017**, *29*, 1606454.